The Astrophysical Journal, 843:146 (12pp), 2017 July 10 https://doi.org/10.3847/1538-4357/aa79a1

Study of the Vertical Magnetic Field in Face-on Galaxies Using Faraday Tomography

Shinsuke Ideguchi[1], Yuichi Tashiro[2], Takuya Akahori[3], Keitaro Takahashi[2], and Dongsu Ryu[1,4]

[1] Department of Physics, UNIST, Ulsan 44919, Korea; ryu@sirius.unist.ac.kr

[2] University of Kumamoto, 2-39-1, Kurokami, Kumamoto 860-8555, Japan

[3] Graduate School of Science and Engineering, Kagoshima University, Kagoshima 890-0065, Japan

[4] Korea Astronomy and Space Science Institute, Daejeon 34055, Korea

Received 2016 December 26; revised 2017 June 8; accepted 2017 June 12; published 2017 July 14

Abstract

Faraday tomography allows astronomers to probe the distribution of the magnetic field along the line of sight (LOS), but that can be achieved only after the Faraday spectrum is interpreted. However, the interpretation is not straightforward, mainly because the Faraday spectrum is complicated due to a turbulent magnetic field; it ruins the one-to-one relation between the Faraday depth and the physical depth, and appears as many small-scale features in the Faraday spectrum. In this paper, by employing "simple toy models" for the magnetic field, we describe numerically as well as analytically the characteristic properties of the Faraday spectrum. We show that the Faraday spectrum along "multiple LOSs" can be used to extract the global properties of the magnetic field. Specifically, considering face-on spiral galaxies and modeling turbulent magnetic field as a random field with a single coherence length, we numerically calculate the Faraday spectrum along a number of LOSs and its shape-characterizing parameters, that is, the moments. When multiple LOSs cover a region of $\gtrsim$(10 coherence length)^2, the shape of the Faraday spectrum becomes smooth and the shape-characterizing parameters are well specified. With the Faraday spectrum constructed as a sum of Gaussian functions with different means and variances, we analytically show that the parameters are expressed in terms of the regular and turbulent components of the LOS magnetic field and the coherence length. We also consider the turbulent magnetic field modeled with a power-law spectrum, and study how the magnetic field is revealed in the Faraday spectrum. Our work suggests a way to obtain information on the magnetic field from a Faraday tomography study.

Key words: galaxies: magnetic fields – methods: numerical – polarization

1. Introduction

Faraday tomography, originally suggested by Burn (1966) and Brentjens & de Bruyn (2005) and replacing the Faraday rotation measure (RM), revolutionized the study of the cosmic magnetic field. This technique creates a tomographic reconstruction of the polarization spectrum as a function of RM or the Faraday depth along the line of sight (LOS). The basic equation is

$$P(\lambda^2) = \int_{-\infty}^{+\infty} F(\phi) e^{2i\phi\lambda^2} d\phi, \quad (1)$$

where $P(\lambda^2)$ is the observed polarization spectrum. Here, $F(\phi)$ is the Faraday spectrum or Faraday dispersion function, which is basically the polarized synchrotron emission due to the "perpendicular" magnetic field, $B_\perp$, as a function of Faraday depth, ϕ. The Faraday depth is defined as

$$\phi(x) = K \int_x^0 n_e(x') B_\parallel(x') dx', \quad (2)$$

where $B_\parallel$ is the "parallel" magnetic field, n_e is the thermal electron density, and x is the physical distance along the LOS. It is given in units of rad m^{-2}. The coefficient is $K = e^3/(2\pi m_e^2 c^4)$, where e is the electron charge, m_e is the electron mass, and c is the speed of light.

The study of magnetic fields using Faraday tomography involves two stages of efforts. One is the reconstruction of $F(\phi)$, and the other is the extraction of magnetic field information from $F(\phi)$. The first requires wide frequency coverage observations of $P(\lambda^2)$, which can be provided by, for instance, the Square Kilometre Array (SKA) and its pathfinders and precursors, such as LOFAR, ASKAP, MeerKAT, MWA, and HERA. Various approaches for it have been suggested (e.g., Sun et al. 2015 and references therein). The second requires a successful interpretation of $F(\phi)$. However, that often turns out to be difficult, because the physical distance is not in a one-to-one correspondence with the Faraday depth owing to the turbulent component of the magnetic field, and thus $F(\phi)$, in general, does not represent the distribution of polarized emission in real space. While it would be straightforward to estimate, for instance, the number of sources of synchrotron radiation and their Faraday depths, the Faraday spectrum could be used to obtain more information. The properties of $F(\phi)$ were previously studied (e.g., Bell et al. 2011; Frick et al. 2011; Beck et al. 2012; Ideguchi et al. 2014). For instance, the characteristic features in $F(\phi)$ caused by various configurations of the large-scale LOS magnetic field such as field reversal were examined using simple models. Also, the effects of a small-scale, turbulent field were taken into account, and how the effects would be superposed on the features due to the large-scale field were studied. It was shown that turbulent field basically appears as many small-scale components in $F(\phi)$, which are called "Faraday forest" (Beck et al. 2012).

In this paper, we extend the second-stage efforts. As the first trial, we consider spiral galaxies and study how the properties of the "vertical" magnetic field (the component vertical to the disk) can be extracted. The strength of the vertical magnetic field is among many yet to be constrained in spiral galaxies (see, e.g., Beck 2016 for a summary). It has been observed in several edge-on galaxies showing the X-shaped pattern (see, e.g., Krause 2009; Beck 2015), but such observations have so far told us mostly only the existence and orientation of the field.

The vertical magnetic field is important for the reconstruction of the global galactic magnetic field and the study of its origin (Sofue et al. 2010), and also necessary to describe cosmic-ray (CR) transportation (galactic wind). In the Milky Way, there is a difference in the strength of the vertical magnetic field toward the north and south Galactic poles, as estimated with RM (Taylor et al. 2009; Mao et al. 2010). This is inconsistent with observations of several external galaxies and needs to be understood (Beck 2016).

Previously, in Ideguchi et al. (2014), we studied the $F(\phi)$ of face-on galaxies, using a realistic model for the Milky Way (Akahori et al. 2013). The model included the global, regular component of the magnetic field, based on observations, as well as the turbulent component, constructed with the data from magnetohydrodynamic turbulence simulations. $F(\phi)$ turned out to be complicated, mostly due to the turbulent magnetic field; it showed the Faraday forest superposed on large-scale diffuse emissions, in agreement with Beck et al. (2012). We also found that $F(\phi)$ can have significantly different shapes for different configurations of the turbulent field, even when the global parameters of the model are fixed. This suggests that while the existence of turbulence can be expected with the Faraday forest, it is not easy to quantify the details of the turbulence. As a matter of fact, turbulence seems to make it difficult to study the global properties of the magnetic field. At the time, our interpretation of $F(\phi)$ was limited because of its complicated behavior. On the other hand, our results indicated that $F(\phi)$ becomes smoother if a larger number of LOSs is used.

We then attempted to extract the properties of the magnetic field using the shape-characterizing parameters of $F(\phi)$, that is, the width, skewness, and kurtosis,

$$\sigma^2 = \frac{\sum_l |F(\phi_l)|(\phi_l - \mu)^2}{\sum_l |F(\phi_l)|} \tag{3}$$

$$\gamma_{\rm s} = \frac{\sum_l |F(\phi_l)|(\phi_l - \mu)^3}{\sigma^3 \sum_l |F(\phi_l)|} \tag{4}$$

$$\gamma_{\rm k} = \frac{\sum_l |F(\phi_l)|(\phi_l - \mu)^4}{\sigma^4 \sum_l |F(\phi_l)|} - 3, \tag{5}$$

where l denotes the lth discretized bin of Faraday depth. Here,

$$\mu = \frac{\sum_l |F(\phi_l)|\phi_l}{\sum_l |F(\phi_l)|} \tag{6}$$

is the spectrum-weighted average of the Faraday depth. We found that stronger vertical magnetic fields result in larger σ; hence, σ should be a useful measure. On the other hand, $\gamma_{\rm s}$ and $\gamma_{\rm k}$ exhibit behaviors that are too complicated. In summary, in Ideguchi et al. (2014), $F(\phi)$ was obtained with a realistic model, but its behavior was not easy to interpret, mainly due to the turbulent field.

After that previous work, we here employ "simple, toy models" for the magnetic field, and try to numerically and analytically describe the behavior of $F(\phi)$. Specifically, for face-on spiral galaxies, we calculate $F(\phi)$ and its shape-characterizing parameters, and examine their dependence on magnetic fields. Even though the models assumed here are simpler than those in former works, they still keep the physical essentials for interpreting $F(\phi)$. Most of all, simple models make analytical interpretation possible. We first employ the turbulent magnetic field described as a random field with a single coherence length. We also consider the turbulent field represented by power-law spectra. We then examine how $F(\phi)$ obtained along "multiple LOSs" can be used to study the vertical magnetic field of face-on spiral galaxies, inspired by the result of Ideguchi et al. (2014) that $F(\phi)$ becomes smoother and thus easier to interpret with a larger number of LOSs. We regard this work as the first step in finding a practical way to extract the magnetic field information from the Faraday spectrum.

In Section 2, we describe our toy model and show the calculated $F(\phi)$. In Section 3, we present the analytical interpretation of $F(\phi)$. In Section 4, we present $F(\phi)$ with a power-law, turbulent magnetic field. The summary and discussion follow in Section 5. Note that in this paper, we concentrate on the characteristics of the "intrinsic" $F(\phi)$, and do not consider observational effects in constructing $F(\phi)$ from $P(\lambda^2)$, such as the ambiguity caused by the limited coverage of observation frequency and observational noises.

2. Faraday Spectrum for Random Magnetic Field with a Single Coherence Length

2.1. Model

We consider a small portion, $\sim(100\,{\rm pc})^2$, of face-on spiral galaxies, and employ a simple model for the galactic magnetic field. The magnetic field is decomposed into parallel ($B_\parallel$) and perpendicular ($B_\perp$) components with respect to the LOS. $B_\parallel$ contributes to the Faraday depth, while $B_\perp$ contributes to polarized synchrotron emission, as mentioned in the Introduction. We further assume that the parallel field is decomposed into random and coherent components, representing the turbulent and global vertical fields, respectively, and express it as

$$\boldsymbol{B}_\parallel = \boldsymbol{B}_{\rm rand} + \boldsymbol{B}_{\rm coh}. \tag{7}$$

From radio polarimetric data of many almost face-on external galaxies, the strength of the turbulent magnetic field is estimated to be 10–15 μG in spiral arms (see, e.g., Beck 2016). So, we set the rms (root-mean-square) strength of $B_{\rm rand}$, σ_B, to be $15/\sqrt{3}$ μG (then, the rms strength of thee three-dimensional (3D) random field is 15 μG). It was shown that the size of turbulent cells in the Galactic disk is $\sim$10–100 pc from a pulsar RM study (Ohno & Shinbata 1993), that the outer scale of the turbulent magnetic field is $\sim$17 pc in the spiral arms and $\sim$100 pc in the interarm regions from an RM study of extragalactic polarized sources (Haverkorn et al. 2006), and that the size of turbulent cells in external galaxies is $\sim$50 pc from a Faraday depolarization study (Beck 2016; see below). Based on these studies, for the coherence length of the random field, we adopt 10 pc as the fiducial value and also consider 50 and 100 pc for comparison. On the other hand, we take $B_{\rm coh}$ as a free parameter, varying its value to see the effects on the Faraday spectrum. Recent RM studies of face-on external galaxies such as IC 342 (Beck 2009) and NGC 628 (Mulcahy et al. 2017) indicated absolute values of the RM up to $\sim$100 rad m^{-2}, which corresponds to up to $\sim$6 μG if we assume that the average thermal electron density along the LOS is 0.02 cm^{-3} and the path length through the thermal gas is 1 kpc. So, we set $B_{\rm coh}$ = 0–5 μG. Note that the positive magnetic field here is meant to be toward the observer, and thus the Faraday depth due to the coherent field is positive.

Regarding the synchrotron radiation, we assume that its polarization angle is the same within the computational domain

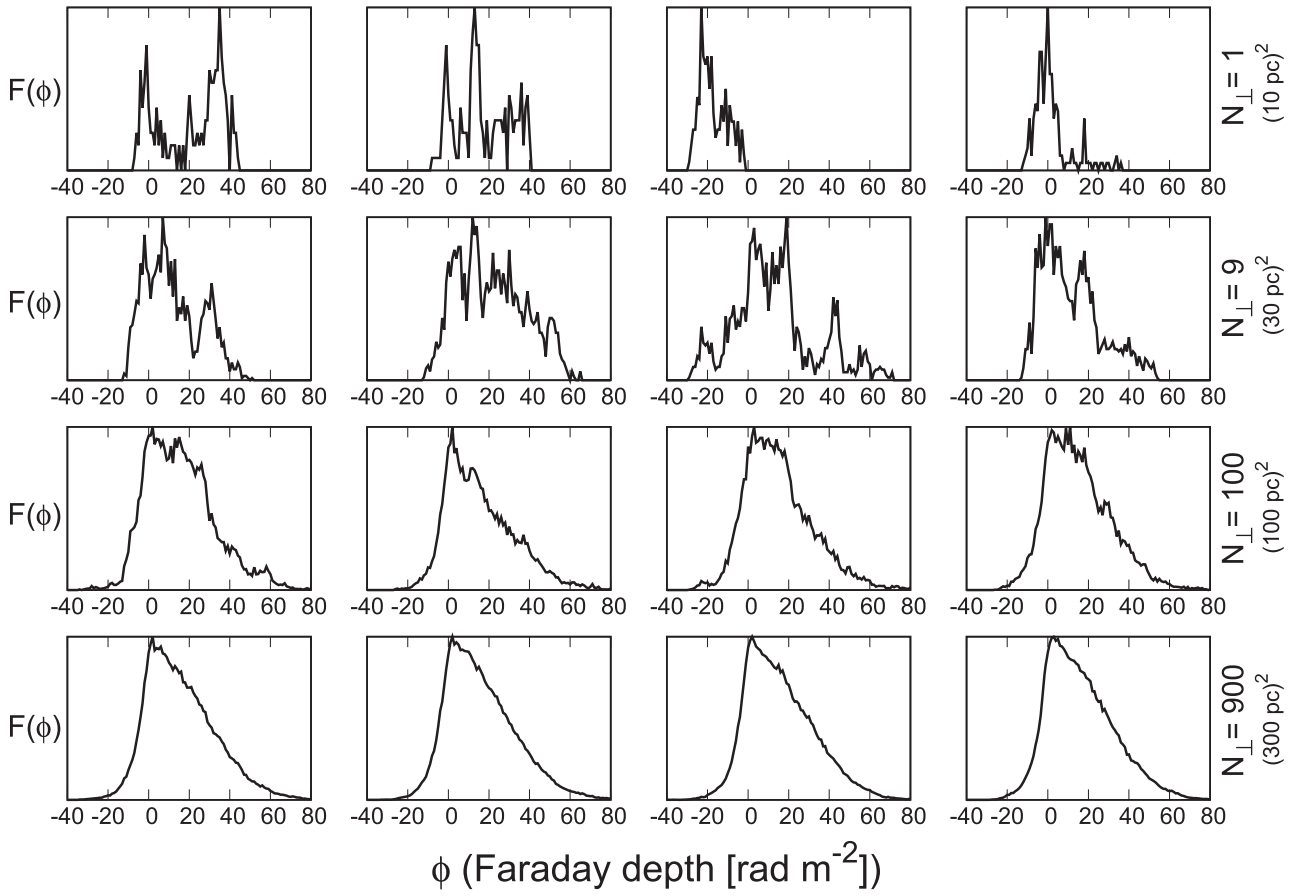

Figure 1. Simulated Faraday spectrum, $F(\phi)$, as a function of Faraday depth, ϕ, with $B_{\rm coh} = 1\ \mu$G, $L_{\rm cell} = 10$ pc, and $L_{\rm SH} = 1$ kpc, for $N_\perp = 1$, 9, 100, and 900 from top to bottom. For each value of $N_\perp$, four different realizations are shown.

(see below). This assumption may be justified with observations of ordered magnetic fields in galactic disks (see, e.g., Beck & Wielebinski 2013). Fletcher et al. (2011), for instance, reported a spiral pattern of $\boldsymbol{B}_\perp$ from polarized radiation in M51, with an angular resolution of 15″, which corresponds to the beam size of ∼500 pc. This means that synchrotron emissions within this beam would have similar polarization angles. From the assumption of same polarization angle, the depolarization caused by the unaligned $B_\perp$ within a magnetized, synchrotron polarization emitting medium (wavelength-independent depolarization) does not occur. In addition, depolarization caused by differential Faraday rotation along the LOS within a medium (Faraday depolarization) and that caused by many polarizations with different angles within an observing beam (beam depolarization) are ignored, which means that an "intrinsic" Faraday spectrum is considered. This is because the emissions that experience certain Faraday rotations are accumulated in the same Faraday depth. Note that the latter two depolarizations occur in $P(\lambda^2)$ space.

Thermal and CR electron densities enter in the calculations of Faraday depth and synchrotron emission. Observations suggest $n_e \sim 0.014$–$0.036\,{\rm cm}^{-3}$ for the thermal electron density in our Galaxy (see, e.g., Gaensler et al. 2008). So, we adopt $n_e = 0.02\,{\rm cm}^{-3}$. We are here concerned only with the overall shape of the Faraday spectrum, but not its amplitude (see Section 2.2). Hence, we do not need to specify the density and energy spectrum of CR electrons nor the strength of the perpendicular magnetic field, $B_\perp$.

The physical quantities described above are assigned to cubic cells of size $L_{\rm cell}$. For $B_{\rm rand}$, we randomly place a $\boldsymbol{B}_0$ of 15 μG strength and take the LOS component. Then, $\sigma_B \equiv \boldsymbol{B}_0/\sqrt{3} = 15/\sqrt{3}\ \mu$G, and the cell size corresponds to the coherence length, that is, $L_{\rm cell} = 10,\ 50,\ 100$ pc. Other quantities, such as $B_{\rm coh}$, n_e, and the synchrotron emissivity, are assumed to be simply uniform in the computational domain.

Along an LOS, we stack up cells for $[-L_{\rm SH}, L_{\rm SH}]$, where $L_{\rm SH}$ is the scale height of the physical quantities. Gaensler et al. (2008), for instance, suggested $L_{\rm SH} \sim$ 430–1830 pc for the thermal electron density in the thick disk of our Galaxy. Krause (2009) reported that the $L_{\rm SH}$ of radio emission, which reflects the $L_{\rm SH}$ of CR electrons and magnetic field, is ∼300 pc for thin disks and ∼1.8 kpc for halos (or thick disks) from observations of various edge-on spiral galaxies. So, we set $L_{\rm SH} = 1$ kpc as the fiducial value and also consider 0.5 and 2 kpc for comparison. Each LOS includes $N_\parallel = 2L_{\rm SH}/L_{\rm cell}$ cells or "layers," that is, 200 layers for representative $L_{\rm cell}$ and $L_{\rm SH}$.

The Faraday spectrum is obtained with $N_\perp$ LOSs, covering a small region in the sky where the properties of the physical quantities can be assumed to be uniform, but still larger than the coherence length of the turbulent magnetic field. We set each layer to consist of $N_\perp = 1^2$–30^2 cells, or the area of $(1^2$–$30^2)L_{\rm cell}^2$. For a representative $L_{\rm cell}$, the area becomes 10^2–300^2 pc^2, which corresponds to, for instance, ∼0.″1–3″ for observations of galaxies in the Virgo Cluster 20 Mpc away.

Our computational domain consists of $N_\parallel \times N_\perp$ cells. With the physical quantities allocated to the cells, we calculate ϕ using Equation (2) and the polarized radiation by adding the

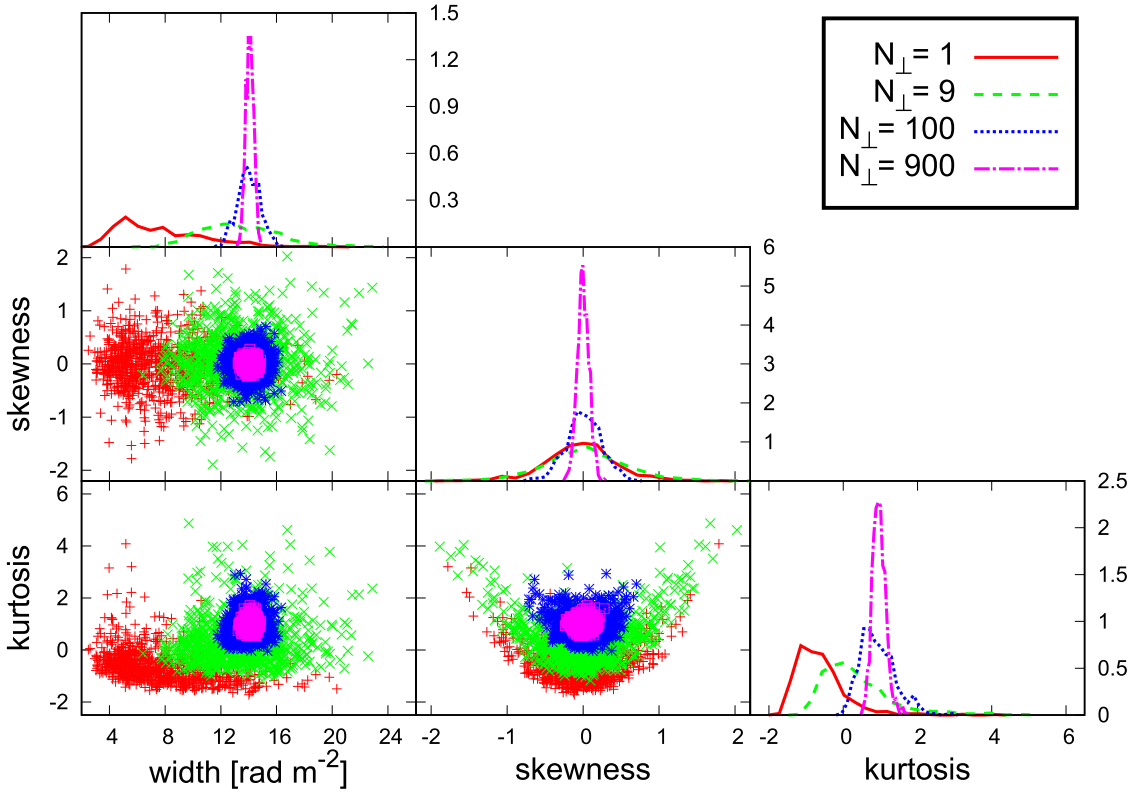

Figure 2. Scatter plots for the shape-characterizing parameters of the Faraday spectrum with $B_{\rm coh} = 0$ μG, $L_{\rm cell} = 10$ pc, and $L_{\rm SH} = 1$ kpc, for $N_\perp = 1$, 9, 100, and 900 shown in red, green, blue, and magenta colors, respectively. Eight hundred realizations are shown. The top plots of each column are the one-dimensional probability distributions of the parameters.

Table 1
Model Parameters

Symbol	Physical Quantities	Adopted Values	Reference
$B_{\rm rand}$	random component of $B_\parallel$	$\sigma_B = 15/\sqrt{3}$ μG	Beck (2016)
$B_{\rm coh}$	coherent component of $B_\parallel$	0–5 μG	Beck (2009), Mulcahy et al. (2017)
n_e	thermal electron density	0.02 cm^{-3}	Gaensler et al. (2008)
$L_{\rm cell}$	cell size	**10**, 50, 100 pc	Ohno & Shinbata (1993), Haverkorn et al. (2006), Beck (2016)
$L_{\rm SH}$	scale height of physical quantities	0.5, **1.0**, 2.0 kpc	Gaensler et al. (2008), Krause (2009)

Note. Fiducial values are denoted in bold.

contribution from cells along the LOSs, so $F(\phi)$. Below we examine the behavior of $F(\phi)$ for different model parameters, including how the shape-characterizing parameters converge as $N_\perp$ increases.

The model parameters are summarized in Table 1. See Section 5 for further discussions of our assumptions.

2.2. Results

2.2.1. Convergence

Figure 1 shows $F(\phi)$ with $B_{\rm coh} = 1$ μG, $L_{\rm cell} = 10$ pc, and $L_{\rm SH} = 1$ kpc (below, representative $L_{\rm cell}$ and $L_{\rm SH}$ are used, unless otherwise stated) for different numbers of LOSs, $N_\perp = 1$, 9, 100, and 900, from top to bottom. Four different realizations of the turbulent magnetic field are shown for each value of $N_\perp$. $F(\phi)$ looks complicated with spikes and varies significantly between different realizations for small $N_\perp$. $F(\phi)$ becomes smooth as $N_\perp$ increases, and converges to a universal shape for $N_\perp \gtrsim 100$. This is because the effects of the random magnetic field on ϕ are statistically averaged out.

As in Ideguchi et al. (2014), the width σ, skewness $\gamma_{\rm s}$, and kurtosis $\gamma_{\rm k}$ of $F(\phi)$ were calculated (see Equations (3)–(5)). Figure 2 shows the scattered distributions of these shape-characterizing parameters with $B_{\rm coh} = 0$ μG for $N_\perp = 1$, 9, 100, and 900; 800 realizations for each value of $N_\perp$ are shown. The convergence of the parameters for large $N_\perp$ is evident. The standard deviation of the width, for instance, decreases as 3.09, 2.72, 0.799, and 0.287 for $N_\perp = 1$, 9, 100, and 900, respectively.

2.2.2. Dependence on $B_{\rm coh}$

Figure 3 shows $F(\phi)$ for $B_{\rm coh} = 0$, 1, 3, and 5 μG, fixing $N_\perp = 100$. The spectrum becomes broader as $B_{\rm coh}$ increases. With $B_{\rm coh} = 0$ μG, only $B_{\rm rand}$ in layers along the LOSs contributes to ϕ by the random walk process. On the other hand, with non-zero $B_{\rm coh}$, there is a contribution due to $B_{\rm coh}$ and the

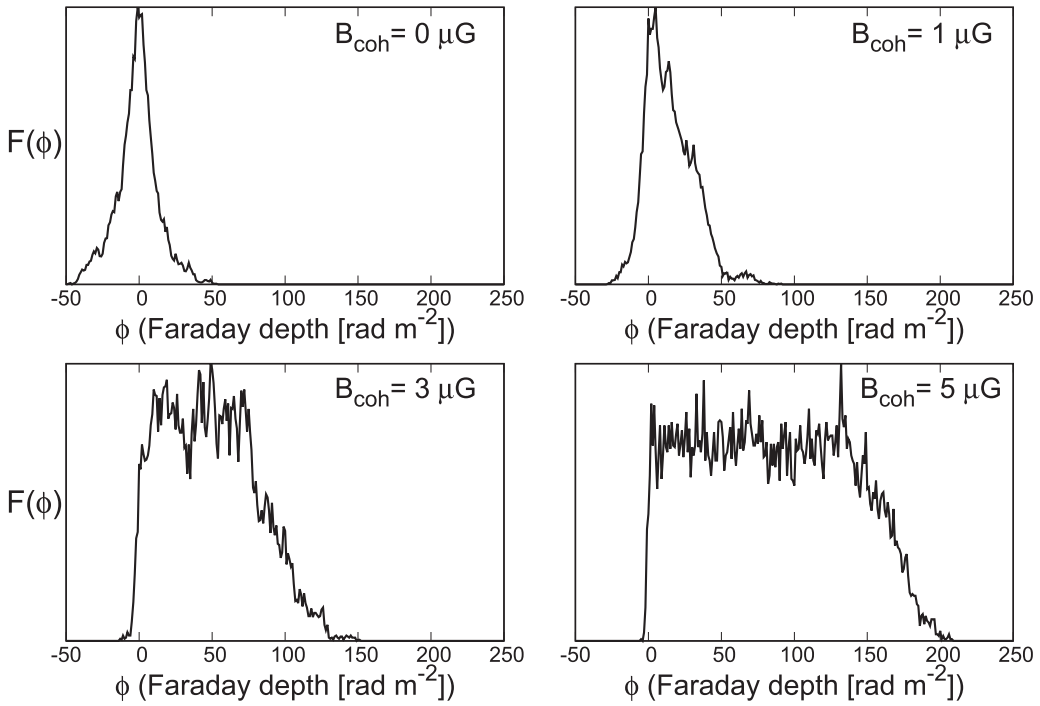

Figure 3. Simulated Faraday spectrum, $F(\phi)$, as a function of Faraday depth, ϕ, with $B_{\rm coh} = 0$, 1, 3, 5 μG; $L_{\rm cell} = 10$ pc, $L_{\rm SH} = 1$ kpc, and $N_{\perp} = 100$.

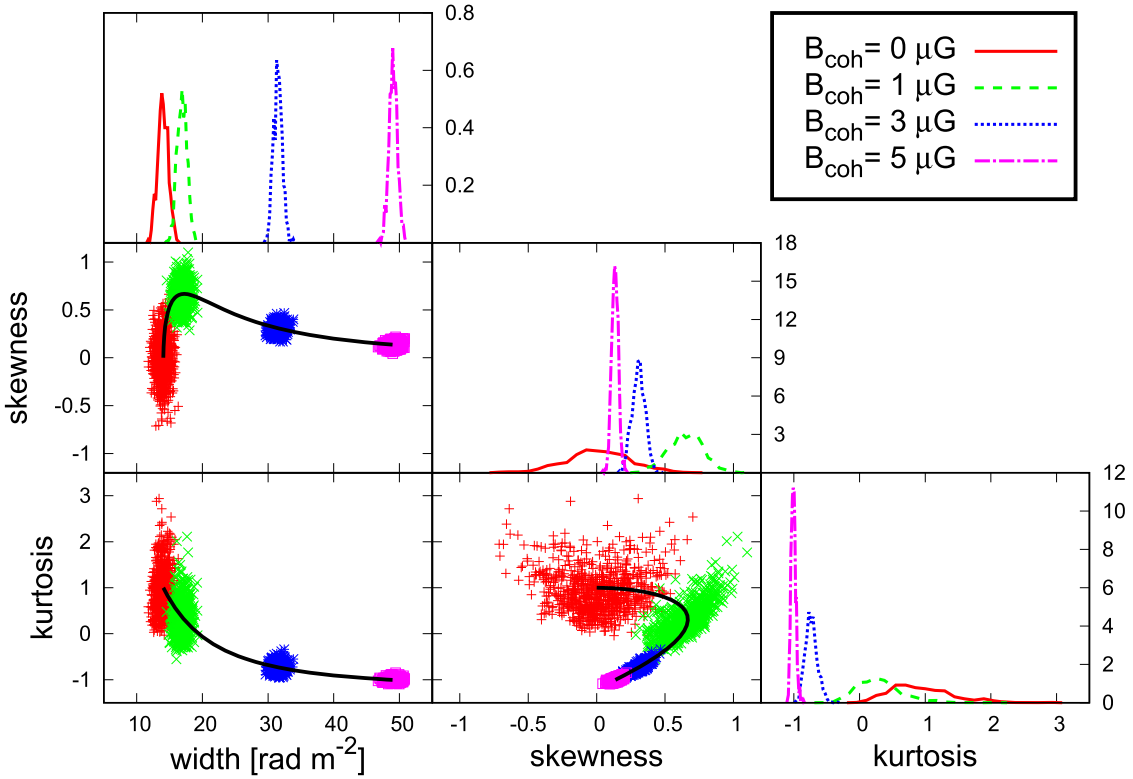

Figure 4. Same as Figure 2, but for $B_{\rm coh} = 0$, 1, 3, 5 μG shown in red, green, blue, and magenta colors, respectively; $L_{\rm cell} = 10$ pc, $L_{\rm SH} = 1$ kpc, and $N_{\perp} = 100$. The overlaid black lines show the analytical solutions (see Section 3) with $B_{\rm coh}$ varying from 0 to 5 μG.

contribution monotonically increases along the LOSs, on top of the contribution due to $B_{\rm rand}$. As a consequence, $F(\phi)$ stretches over a large range of ϕ. The stretching is larger for larger $B_{\rm coh}$.

Figure 4 shows the distributions of the shape-characterizing parameters for $B_{\rm coh} = 0$, 1, 3, and 5 μG, fixing $N_{\perp} = 100$. The parameters change systematically with $B_{\rm coh}$. For $B_{\rm coh} = 0$ μG, $F(\phi)$ has small σ, as explained. The narrow, sharp (leptokurtic) shape results in a positive $\gamma_{\rm k}$, while the symmetric shape causes $\gamma_{\rm s}$ to be zero. As $B_{\rm coh}$ increases, σ increases. At the same time, a flat region appears in $F(\phi)$ (see the 5 μG case in Figure 3), and hence the shape changes from leptokurtic to platykurtic, so $\gamma_{\rm k}$ becomes negative. The change in $\gamma_{\rm s}$, on the other hand, is

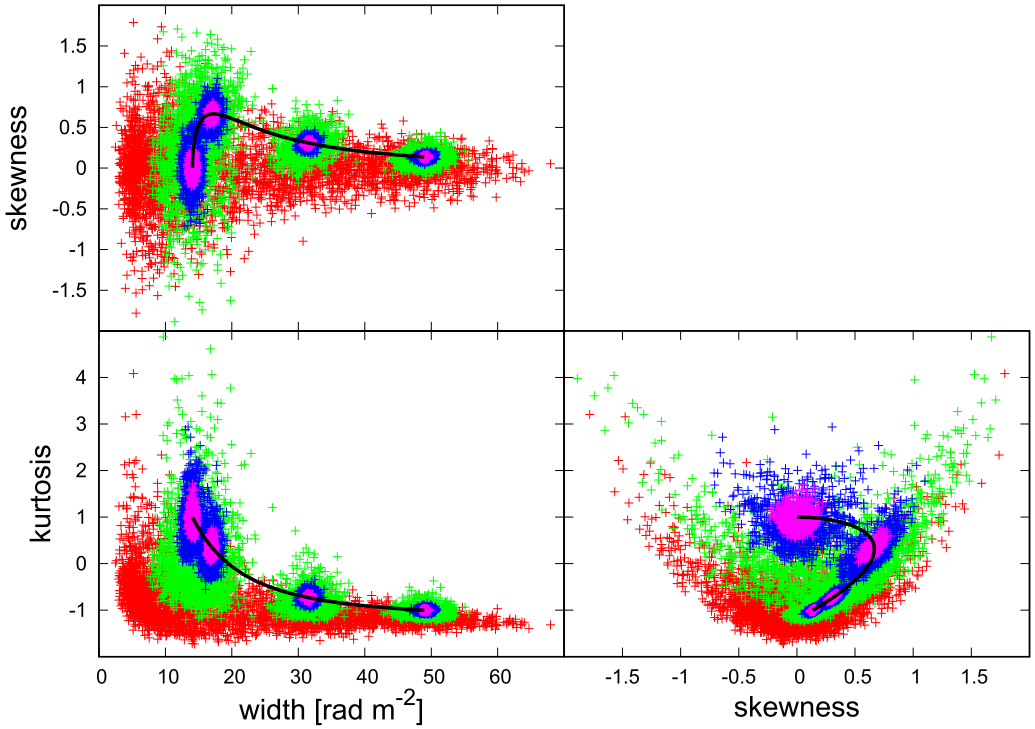

Figure 5. Same as Figure 4, but for $N_\perp = 1$, 9, 100, and 900 shown in red, green, blue, and magenta colors, respectively. The parameters for different $B_{\rm coh}$ but same $N_\perp$ are plotted with the same color. The overlaid black lines for the analytical solutions are the same as those in Figure 4. One-dimensional distributions are not shown.

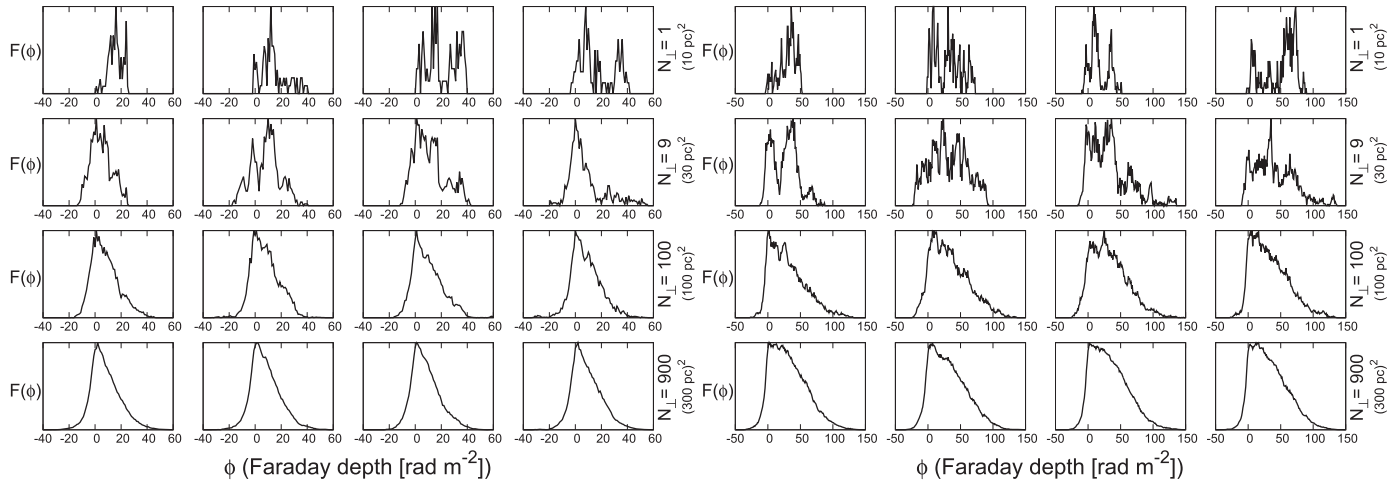

Figure 6. Same as Figure 1, but with $L_{\rm SH} = 0.5$ kpc (left) and 2.0 kpc (right); $B_{\rm coh} = 1$ μG and $L_{\rm cell} = 10$ pc.

not monotonic. For a non-zero but small $B_{\rm coh}$, $F(\phi)$ becomes positively skewed and $\gamma_{\rm s}$ increases. For larger $B_{\rm coh}$, the flat region restores the symmetry about the mean, causing $\gamma_{\rm s}$ to decrease. These behaviors of $F(\phi)$ and the shape-characterizing parameters will be quantitatively described in Section 3. Figure 5 shows the convergence of the shape-characterizing parameters for increasing $N_\perp$. The parameters are reasonably converged, again for $N_\perp \gtrsim 100$. This indicates that the observation covering a region $\gtrsim$100 times the square of the coherence length of the turbulent magnetic field would be useful to extract information on the magnetic field.

2.2.3. Dependence on $L_{\rm SH}$ and $L_{\rm cell}$

Figure 6 compares $F(\phi)$ for $L_{\rm SH} = 0.5$ and 2.0 kpc; the other parameters are $B_{\rm coh} = 1$ μG and $L_{\rm cell} = 10$ pc. The change in $L_{\rm SH}$ affects the number of cells (or the number of coherence lengths of turbulent magnetic field) along the LOS: $N_\parallel = 100$ for $L_{\rm SH} = 0.5$ kpc and $N_\parallel = 400$ for $L_{\rm SH} = 2.0$ kpc. $F(\phi)$ converges to universal shapes for $N_\perp \gtrsim 100$ as before, but the shapes are different for different $L_{\rm SH}$, because ϕ spans a larger range with larger $L_{\rm SH}$.

Figure 7 compares $F(\phi)$ for $L_{\rm cell} = 50$ and 100 pc; the other parameters are $B_{\rm coh} = 1$ μG and $L_{\rm SH} = 1.0$ kpc. The number of cells along the LOS is $N_\parallel = 40$ for $L_{\rm cell} = 50$ pc and $N_\parallel = 20$ for $L_{\rm cell} = 100$ pc. The figure shows $F(\phi)$ with $N_\perp$ corresponding to the covering area of (100 pc)^2 ($N_\perp = 4$ for $L_{\rm cell} = 50$ pc and $N_\perp = 1$ for $L_{\rm cell} = 100$ pc) and (300 pc)^2 ($N_\perp = 36$ for $L_{\rm cell} = 50$ pc and $N_\perp = 9$ for $L_{\rm cell} = 100$ pc) to be compared with that for $L_{\rm cell} = 10$ pc, as well as $F(\phi)$ with $N_\perp = 100$ and 900. For convergence, again $N_\perp \gtrsim 100$ is required. But for $L_{\rm cell} = 100$ pc, even $N_\perp = 100$ does not produce a smooth

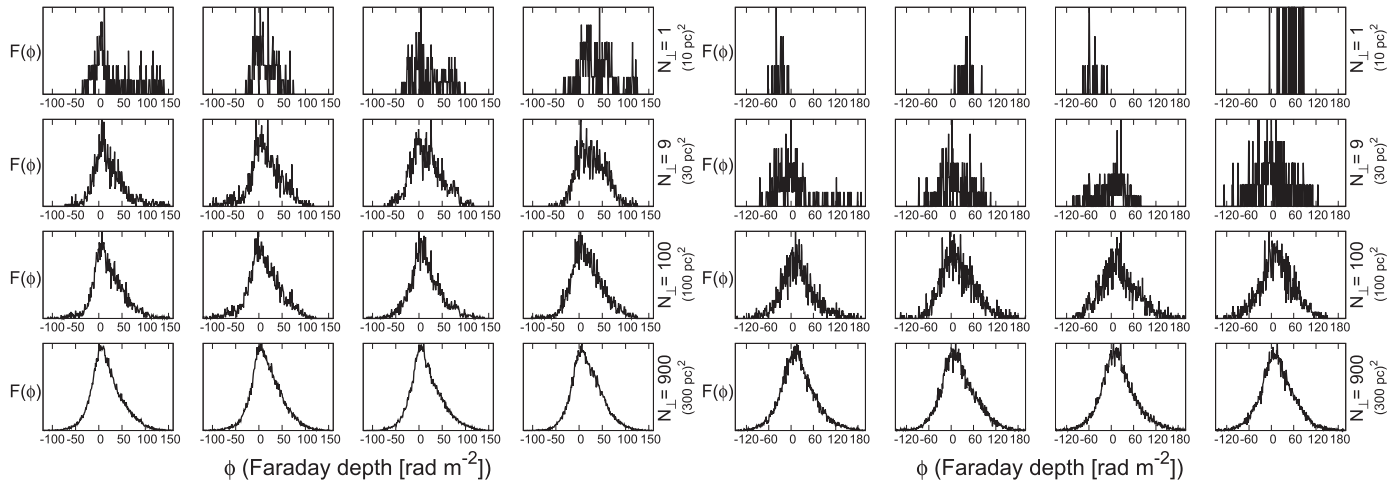

Figure 7. Same as Figure 1, but with $L_{\rm cell} = 50$ pc (left) and 100 pc (right); $B_{\rm coh} = 1$ μG and $L_{\rm SH} = 1$ kpc.

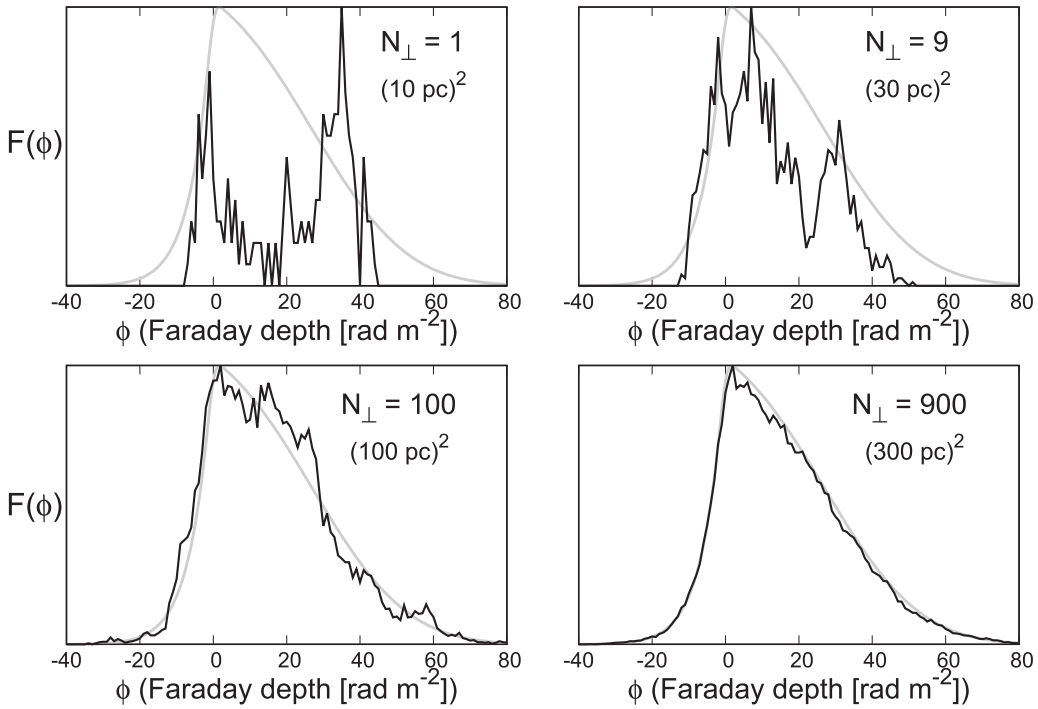

Figure 8. Simulated Faraday spectrum, $F(\phi)$, as a function of Faraday depth, ϕ, for $N_\perp = 1$, 9, 100, and 900 (black lines), overlaid with the analytically reproduced spectrum (gray lines); $B_{\rm coh} = 1$ μG, $L_{\rm cell} = 10$ pc, and $L_{\rm SH} = 1$ kpc. The simulated spectra are the same as those in Figure 1, but with different realizations.

$F(\phi)$, because $N_\parallel$ is too small or the path length does not include enough number of coherence lengths. The converged shape, on the other hand, only weakly depends on $L_{\rm cell}$.

3. Analytic Faraday Spectrum

We next analytically derive $F(\phi)$ and the shape-characterizing parameters in the limit of large $N_\perp$, or large numbers of LOSs, and interpret the results presented in the previous section. The Faraday depth up to the nth layer along the LOS can be written as

$$\phi_n = \sum_{j=1}^{n} (\Delta\phi_{\rm coh} + \Delta\phi^j_{\rm rand}) = n\Delta\phi_{\rm coh} + \sum_{j=1}^{n} \Delta\phi^j_{\rm rand}. \quad (8)$$

Here, $\Delta\phi_{\rm coh} = Kn_e B_{\rm coh} L_{\rm cell}$ is the contribution from the coherent component of $B_\parallel$, which is the same for all layers; $\Delta\phi^j_{\rm rand} = Kn_e B^j_{\rm rand} L_{\rm cell}$ is from the random component of the jth layer. The mean and variance of the random parts are

$$\left\langle \sum_{j=1}^{n} \Delta\phi^j_{\rm rand} \right\rangle = 0 \quad (9)$$

$$\left\langle \left(\sum_{j=1}^{n} \Delta\phi^j_{\rm rand} \right)^2 \right\rangle = \left\langle \sum_{j=1}^{n} (\Delta\phi^j_{\rm rand})^2 \right\rangle = n\sigma^2_\phi, \quad (10)$$

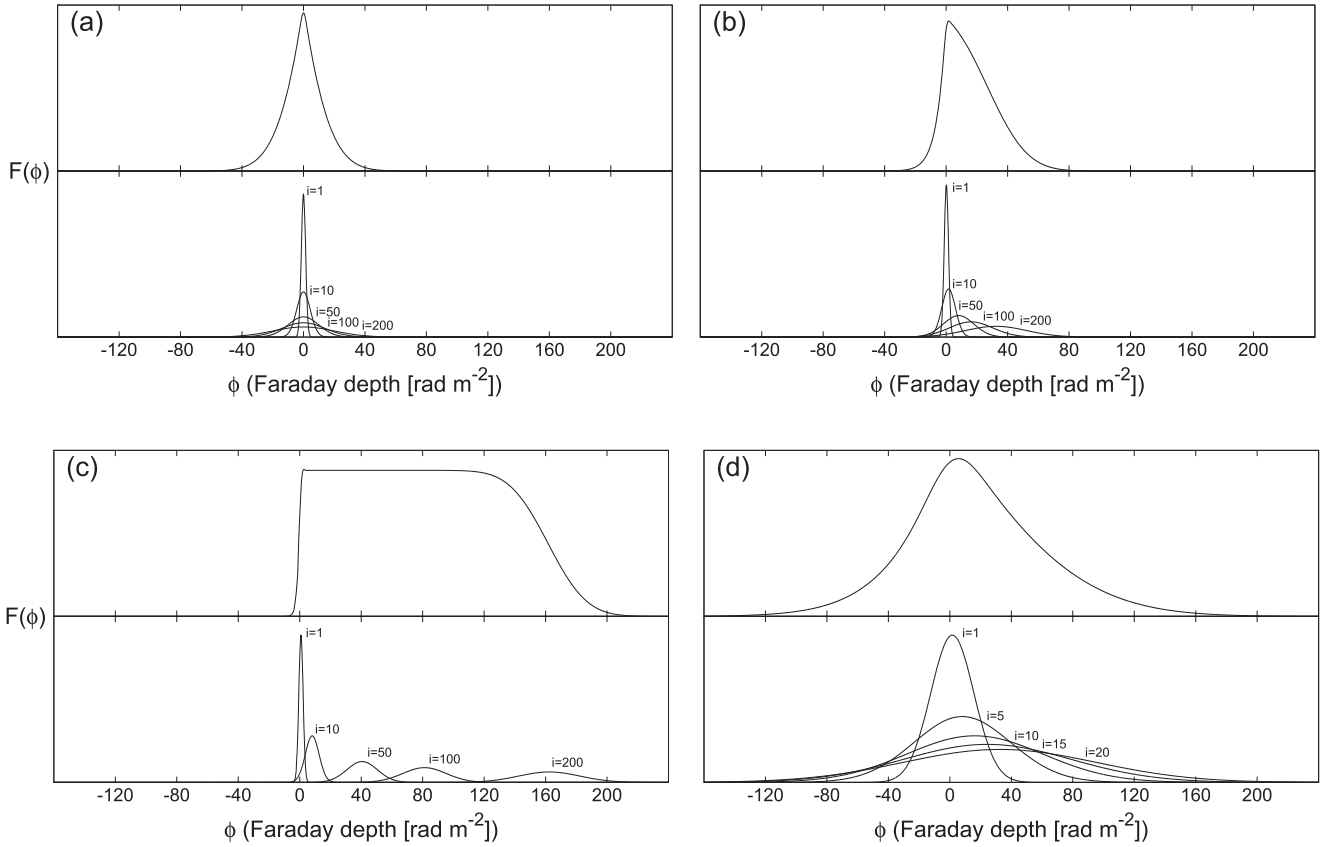

Figure 9. Analytical Faraday spectra with ($L_{\rm cell}$[pc], $B_{\rm coh}$[μG]) = (10, 0), (10, 1), (10, 5), and (100, 1), shown in (a), (b), (c), and (d), respectively; $L_{\rm SH}$ = 1 kpc. The lower parts of the panels show contributions from a number of different layers using Equation (12). The spectra in the upper parts are the sums of the contributions along the LOS.

where $\sigma_\phi^2 = K^2 n_e^2 \sigma_B^2 L_{\rm cell}^2$ with $\langle B_{\rm rand}^2 \rangle = \sigma_B^2$. We assume that there is no correlation between the $B_{\rm rand}$ of the different layers.

We further assume that the polarized synchrotron emissivity and the polarization angle are uniform throughout the computational domain (see Section 2.1). Then, the jth layer's contribution to the Faraday spectrum, $P_j(\phi)$, is proportional to the probability distribution of the Faraday depth of the jth layer, and $F(\phi)$, aside from the overall normalization, is given by

$$F(\phi) \propto \sum_{j=1}^{N_\parallel} P_j(\phi). \tag{11}$$

The functional form of $P_j(\phi)$ reflects the characteristics of the probability distribution. In the limit of large $N_\perp$, the central limit theorem dictates that $P_j(\phi)$ approaches the normal distribution with $j\Delta\phi_{\rm coh}$ as the mean and $j\sigma_\phi^2$ as the variance:

$$P_j(\phi) = \frac{1}{\sqrt{2\pi j}\,\sigma_\phi} \exp\left[-\frac{(\phi - j\Delta\phi_{\rm coh})^2}{2j\sigma_\phi^2}\right]. \tag{12}$$

That is, the Faraday spectrum is approximated as a sum of many Gaussian functions with different means and variances. Figure 8 shows the comparisons of the simulated $F(\phi)$ with the spectrum in Equations (11) and (12) for $B_{\rm coh} = 1\ \mu$G. As $N_\perp$ increases, the statistical fluctuations due to the turbulence magnetic field are reduced and the simulated $F(\phi)$ approaches the analytical solution.

Figure 9 illustrates how the specific shape of $F(\phi)$ is induced for different parameters of ($L_{\rm cell}$[pc], $B_{\rm coh}$[μG]) = (10, 0), (10, 1), (10, 5), and (100, 1) in panels (a), (b), (c), and (d), respectively. When $B_{\rm coh} = 0\ \mu$G, the contribution from each layer is the Gaussian with zero mean, but the variance increases with increasing j. As a consequence, $F(\phi)$ becomes symmetric about $\phi = 0$ with zero skewness and leptokurtic with positive kurtosis (see also Figure 3). With non-zero $B_{\rm coh}$, the mean of the Gaussian also increases as j increases. So, $F(\phi)$ becomes skewed toward positive ϕ, and the shape changes from leptokurtic to platykurtic as $B_{\rm coh}$ increases, as shown in Figures 9(b) and (c) (also in Figure 3). In the figures, $F(\phi)$ for a large positive ϕ represents emissions from the far side of the computational box. Their contributions to a large ϕ are small, because emissions from the far side experience Faraday rotation due to the turbulent fields in nearer layers and spread out in ϕ space. We note that the polarization angle of emissions is assumed to be uniform in our model, and any depolarizations are not included in our calculation (see Section 2.1). For $B_{\rm coh}$ comparable to or larger than σ_B, $F(\phi)$ stretches over a large range of ϕ, and the skewness decreases. For larger $L_{\rm cell}$, shown in Figure 9(d), the variance from each layer is larger, but the number of layers is smaller. Thus, the shape becomes relatively more symmetric.

Once the Faraday spectrum is given as in Equations (11) and (12), the width, skewness, and kurtosis can be analytically

calculated as (see the Appendix)

$$\sigma^2 = \frac{N_\parallel^2 - 1}{12}\Delta\phi_{\rm coh}^2 + \frac{N_\parallel + 1}{2}\sigma_\phi^2 \rightarrow \frac{N_\parallel^2}{12}\Delta\phi_{\rm coh}^2 + \frac{N_\parallel}{2}\sigma_\phi^2 = \frac{K^2 n_e^2 N_\parallel L_{\rm cell}^2}{12}(N_\parallel B_{\rm coh}^2 + 6\sigma_B^2), \quad (13)$$

$$\gamma_{\rm s} = \frac{N_\parallel(N_\parallel^2 - 1)\Delta\phi_{\rm coh}\sigma_\phi^2}{4\left[\frac{N_\parallel^2-1}{12}\Delta\phi_{\rm coh}^2 + \frac{N_\parallel+1}{2}\sigma_\phi^2\right]^{3/2}} \rightarrow \frac{6\sqrt{3N_\parallel}B_{\rm coh}\sigma_B^2}{(N_\parallel B_{\rm coh}^2 + 6\sigma_B^2)^{3/2}} = {\rm sign}(B_{\rm coh})\frac{6\sqrt{3}\sqrt{\alpha}}{(\alpha+6)^{3/2}}, \quad (14)$$

$$\gamma_{\rm k} = \frac{-\frac{N_\parallel^4-1}{120}\Delta\phi_{\rm coh}^4 + \frac{N_\parallel^2-1}{4}\sigma_\phi^4}{\left[\frac{N_\parallel^2-1}{12}\Delta\phi_{\rm coh}^2 + \frac{N_\parallel+1}{2}\sigma_\phi^2\right]^2} \rightarrow -\frac{6}{5}\frac{N_\parallel^2 B_{\rm coh}^4 - 30\sigma_B^4}{(N_\parallel B_{\rm coh}^2 + 6\sigma_B^2)^2} = -\frac{6}{5}\frac{\alpha^2 - 30}{(\alpha+6)^2}, \quad (15)$$

where "$\rightarrow$" denotes the limit of $N_\parallel \gg 1$ ($N_\parallel$ = 10–400 in our model; see Section 2) and $\alpha = N_\parallel B_{\rm coh}^2/\sigma_B^2$. The black lines of Figures 4 and 5 show these analytical solutions, which well reproduce the simulated results.

We learn the following. (i) The width increases with increasing $B_{\rm coh}$, σ_B, and coherence length $L_{\rm cell}$. (ii) Both the skewness and kurtosis are expressed with a single parameter, $\alpha = N_\parallel B_{\rm coh}^2/\sigma_B^2$, which represents the relative importance of coherent to random fields (see Equations (8) and (10)). (iii) The skewness is zero for $\alpha = 0$ and also for $\alpha \rightarrow \infty$, and its sign is determined by the sign of $B_{\rm coh}$. (iv) The kurtosis changes from +1 (leptokurtic) for $\alpha = 0$ to $-6/5$ (platykurtic) for $\alpha \rightarrow \infty$. Hence, if the width, skewness, and kurtosis of $F(\phi)$ are obtained from observations, we may be able to get the information such as the strengths of the global and random components of the magnetic field parallel to LOSs as well as the coherence length of the turbulent magnetic field (see Section 5). We point out that the shape-characterizing parameters of the "intrinsic" $F(\phi)$ are expressed with $N_\parallel$, $B_{\rm coh}$, and σ_B as shown in Equations (13)–(15) and do not depend on the observation frequency coverage.

4. Faraday Spectrum for the Turbulent Magnetic Field with Power-law Energy Spectrum

We also consider a magnetic field model that is a bit more realistic, where the turbulent magnetic field is represented by the energy spectrum of two power laws, such as

$$\begin{cases} E_B(k) \propto k^\alpha & (k \leqslant k_{\rm innner}) \\ E_B(k) \propto k^\beta & (k > k_{\rm inner}). \end{cases} \quad (16)$$

The outer scale in real space (which corresponds to an inner scale in Fourier space), $L_{\rm outer} \equiv 2\pi/k_{\rm inner}$, is set to be 10–100 pc (see Section 2.1). The slope for $k \leqslant k_{\rm inner}$, α, is fixed as 2 (see, e.g., Lesieur 1997), while for $k > k_{\rm inner}$, a range of values, $-2 \leqslant \beta \leqslant -1.5$, is considered. $\beta = -5/3$ is the Kolmogorov slope, which is close, for instance, to the power spectrum slope of the interstellar electron density (see, e.g., Armstrong et al. 1981).

In a box of size $L_{\rm box} = 2$ kpc, divided into $(512)^3$ grid zones (so that the grid size is ~4 pc), a 3D turbulent magnetic field is constructed, as follows. The Fourier components, satisfying $\boldsymbol{k} \cdot \boldsymbol{B}_k$ (and so ensuring $\boldsymbol{\nabla} \cdot \boldsymbol{B} = 0$ in real space), are drawn from a Gaussian random field in Fourier space. Their relative amplitudes are determined by the above spectrum. The components are converted into quantities in real space by Fourier transformation and then added. The absolute amplitude is tuned in such a way that the resulting 3D magnetic field has the rms value of 15 μG. Then, the LOS component is taken as $B_{\rm rand}$, which has $\sigma_B = 15/\sqrt{3}$ μG. The thermal electron density n_e, synchrotron emissivity, and polarization angle are assumed to be uniform within the computational domain, as in Section 2.

Figure 10 shows the simulated $F(\phi)$ with $B_{\rm coh}$ = 0, 1, and 5 μG from top to bottom for different $L_{\rm outer}$ and β. The profiles of $F(\phi)$ are smooth, since $F(\phi)$ is obtained with $N_\perp = 512^2$ covering a $(2\,{\rm kpc})^2$ region. Although not shown here, once the covering region is sufficiently large, specifically, larger than $\sim(10L_{\rm int})^2$ (see below for the definition of $L_{\rm int}$), $F(\phi)$ converges, similar to that discussed in Section 2. The shape of $F(\phi)$ changes sensitively with changing $B_{\rm coh}/\sigma_B$, as well as with changing $L_{\rm outer}$. On the other hand, the dependence on β is weak in the range of β considered.

The black lines of Figure 10 show the analytically constructed $F(\phi)$ of Section 3 with the integral scale length,

$$L_{\rm int} = 2\pi\int\frac{E_B(k)}{k}dk \Big/ \int E_B(k)dk, \quad (17)$$

for $\beta = -5/3$, as the coherence length (that is, the $L_{\rm int}$ used for $L_{\rm cell}$ in Equations (11) and (12)), and correspondingly, with $N_\parallel = L_{\rm box}/L_{\rm int}$. Note that $L_{\rm int}$ = 0.5–0.75 $L_{\rm outer}$ for $-2 \leqslant \beta \leqslant -1.5$. The analytically constructed spectra fit well the simulated ones. This is expected, since it is known that the variance of RM can be expressed with $L_{\rm int}$ for the coherence length of the turbulent magnetic field (see, e.g., Cho & Ryu 2009). This result implies that even if the turbulent part of the galactic magnetic field is described by power-law spectra, once a smooth profile of $F(\phi)$ is obtained through observations of multiple LOSs, the width, skewness, and kurtosis may be used to retrieve the strength of the global and random components of $B_\parallel$ as well as the integral scale length of the turbulent magnetic field.

5. Summary and Discussion

The study of the cosmic magnetic field using Faraday tomography involves not only the reconstruction of the Faraday spectrum, $F(\phi)$, through observations of the polarization spectrum, but also the extraction of magnetic field information from $F(\phi)$. The latter part, however, often turns out to be complicated, mainly because of the turbulent component of the magnetic field; it causes the relation between the Faraday depth and the physical depth to be non-trivial and produces the Faraday forest (Frick et al. 2011; Beck et al. 2012), many small-scale features, in $F(\phi)$. Our previous work (Ideguchi et al. 2014)

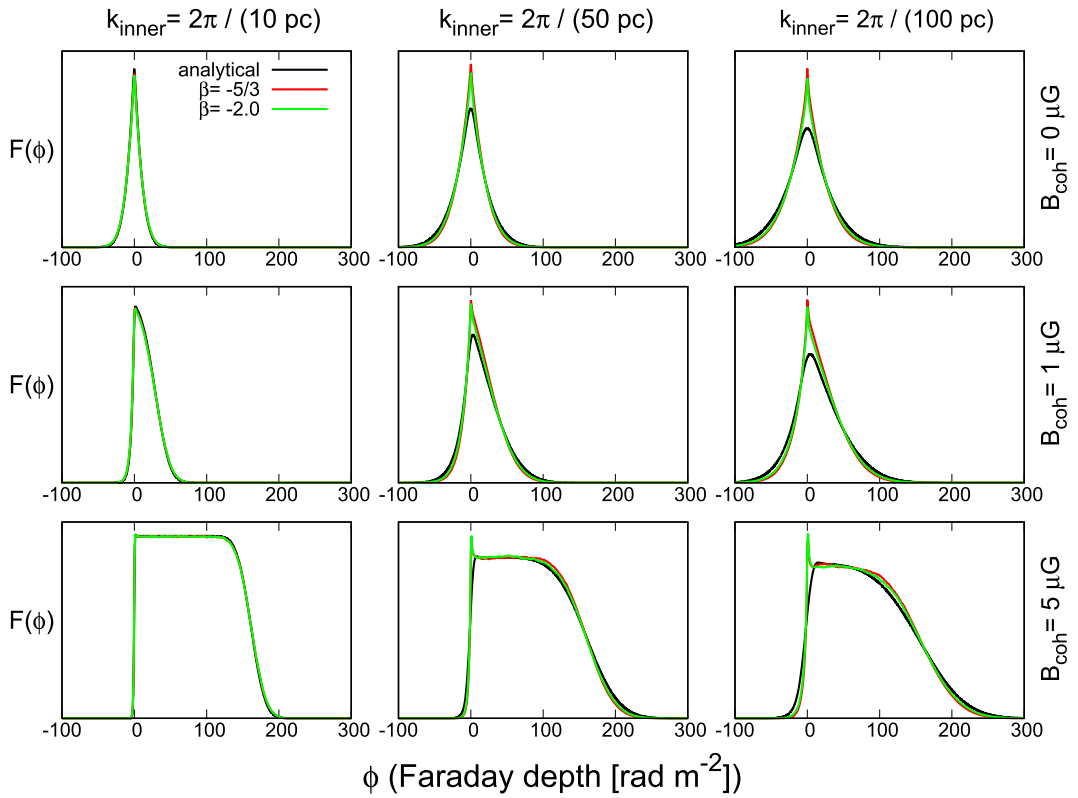

Figure 10. Simulated Faraday spectrum, $F(\phi)$, as a function of Faraday depth, ϕ, for the turbulent magnetic field reproduced with power-law spectra; $B_{\rm coh} = 0$, 1, 5 μG from top to bottom, and $\sigma_B = 15/\sqrt{3}$ μG. The spectra with different outer scales, $L_{\rm outer}$, and power-law slopes, β, are shown. The black lines are the analytic spectra of Section 3 for $\beta = -5/3$. See the main text for further details.

showed that $F(\phi)$ calculated with a realistic model for the Milky Way (Akahori et al. 2013) has the Faraday forest superposed on the large-scale diffuse emission. We also found that $F(\phi)$ can have significantly different shapes for different configurations of turbulence, despite the global parameters of the model being fixed. But in Ideguchi et al. (2014), the interpretation of $F(\phi)$ was limited, due to its complicated behavior. In this work, we studied the $F(\phi)$ of face-on spiral galaxies with the magnetic fields described with simpler, toy models, and tried to numerically as well as analytically interpret $F(\phi)$. We investigated how $F(\phi)$ along multiple LOSs, covering a small region where the properties of the magnetic field and other quantities such as thermal and CR electron densities are assumed to be uniform, can be used in Faraday tomography study.

With the turbulent magnetic field described as a random field with a single coherence length, we numerically showed that small-scale features in $F(\phi)$ are smoothed out and the shape of $F(\phi)$ converges, if $F(\phi)$ is obtained with LOSs covering a region of $\gtrsim$(10 coherence length)^2 in the sky. Note that this explains why we failed to obtain a converged $F(\phi)$ in Ideguchi et al. (2014); with $L_{\rm int} \sim 75$ pc, the covering region of $(500\,{\rm pc})^2$ is smaller than the requirement for convergence. Also note that we do not need very high angular resolutions of radio interferometers to apply this method, in the sense that the observed field should be much larger than the coherence length of the turbulent field to smooth out the small-scale features in $F(\phi)$.

We then analytically showed that the converged $F(\phi)$ can be expressed as a sum of Gaussian functions with $j\Delta\phi_{\rm coh}$ as the mean and $j\sigma_\phi^2$ as the variance along LOSs; $j\Delta\phi_{\rm coh}$ is the RM up to the jth layer due to the coherent component of $B_\parallel$, $B_{\rm coh}$, and $j\sigma_\phi^2$ is the variance of RM due the random component of $B_\parallel$, $B_{\rm rand}$. The analytical expression was derived using the central limit theorem. Then, the shape-characterizing parameters, that is, the width, skewness, and kurtosis of $F(\phi)$, are given as simple functions of the strength of $B_{\rm coh}$ and the variance and coherence length of $B_{\rm rand}$.

With the turbulent magnetic field reproduced with power-law spectra, the same results are obtained, once the coherence length is replaced with the integral length of the turbulent magnetic field.

Our results suggest a way to extract quantities such as the strength and coherence length of the vertical magnetic field in face-on spiral galaxies with Faraday tomography. We point that the $F(\phi)$ along a single LOS and the $F(\phi)$ constructed with multiple LOSs can be used differently. While the $F(\phi)$ along a single LOS can tell us, for instance, about the existence of a turbulent field, the $F(\phi)$ along multiple LOSs can provide us with the global properties of the magnetic field such as the strength and coherence length.

Our analytic expressions could be used to interpret the results of other works. For instance, Frick et al. (2011) calculated $F(\phi)$ including both regular and turbulent fields, and obtained a small skewness. They assumed a Gaussian distribution of the large-scale field with the peak strength of $\sim$2.0 μG, and the rms value of a small-scale turbulent field with a Kolmogorov spectrum is twice that of large-scale field. If we estimate $N_\parallel = 200$, $B_{\rm coh} = 2.0$ μG, and $\sigma_B^2 = 16/3$ $(\mu{\rm G})^2$ (so that the rms strength of the random field is 4 μG) for simplicity, $\alpha \sim 150$. From Equation (14), note that the skewness is large only for α around unity, that is, only when the contributions of

the coherent and turbulent fields to ϕ are comparable. The models adopted in Frick et al. (2011) result in small skewness, i.e., $\gamma_s \sim 0.065$ for $\alpha \sim 150$, mainly because the contribution of the coherent field is much larger than that of turbulent field.

The α parameter is composed of three quantities, $N_{\parallel}$, $B_{\rm coh}$, and σ_B. While it would be useful if we could separate them from observables such as skewness and kurtosis, that is not easy mainly because the quantities are degenerate. For instance, any combination of three quantities providing the same α value results in the same skewness and kurtosis. However, the width of $F(\phi)$ is large if $N_{\parallel}$ and $B_{\rm coh}$ are large, regardless of the σ_B value. Hence, we may be able to understand how the three parameters depend on the shape-characterizing parameters. We will leave the exploration of this to a future work.

In this work, we ignored the possible differences between disk and halo (or thick disk). Observations suggested that the halo magnetic field would have a topology very different from that of a disk (e.g., Fletcher et al. 2011). If the component of the halo magnetic field parallel to the LOS is mostly turbulent, such a field may lead to Faraday dispersion, which broadens and weakens the signals seen in $F(\phi)$, and $F(\phi)$ would become more complicated. If the component is mostly coherent and the halo does not contribute to polarized emission, $F(\phi)$ only shifts in ϕ space. The impact of the halo on $F(\phi)$ will depend on the amount of polarized emission. If the halo emission is as large as that of the disk, the observed spectrum may suffer substantial wavelength-independent depolarization, since the perpendicular components of the halo and disk fields would in general not be aligned with each other. However, observations showed that the distribution of radio emission from halos of edge-on spiral galaxies can be described by an exponential function, for instance, with the scale heights of about 1.8 kpc (Krause 2009). This suggests that the halo emission is small compared to that of the disk.

Finally, we consider the work presented here to be the first step toward understanding the intrinsic characteristics of $F(\phi)$, and thus it needs to be become more sophisticated with more realistic treatments of the galactic magnetic field. In addition, when $F(\phi)$ is constructed from an observed polarization spectrum, effects such as a false signal in RM CLEAN (Farnsworth et al. 2011; Kumazaki et al. 2014; Miyashita et al. 2016) as well as the limited frequency coverage and noises in observation need to be considered. For instance, the shape of $F(\phi)$ could depend on the wavelength because of an imperfect Fourier transform due to the limited sampling of the squared wavelength. Also, the resolution in Faraday depth space, which is determined by the λ^2 coverage (Brentjens & de Bruyn 2005), becomes important for the method presented here to be applied. In the case of a large $B_{\rm coh}$, like 5 μG (e.g., Figure 9(c)), a resolution of $\lesssim$ a few 10 rad m^{-2} may be enough to calculate the shape-characterizing parameters. The full ASKAP (700–1800 MHz), giving a $\sim$22 rad m^{-2} resolution, would then be good enough. On the other hand, when $B_{\rm coh}$ is smaller, like 1 μG (e.g., Figure 9(b)), a resolution of $\lesssim$10 rad m^{-2} seems to be necessary. Upgraded GMRT (e.g., 300–900 MHz), which gives a $\sim$4 rad m^{-2} resolution, could then be used. Furthermore, if we try to apply the method to galaxies with much weaker fields such as the Milky Way, where the vertical $B_{\rm coh}$ at the solar radius is up to $\sim$0.3 μG (Taylor et al. 2009; Mao et al. 2010) and the random field is $\sim$5 μG (Orlando & Strong 2013) toward the direction of the Galactic poles, we need a much higher resolution due to the smaller width of $F(\phi)$. Hence, LOFAR (e.g., 120–240 MHz, high frequency band), giving a $\lesssim$1 rad m^{-2} resolution, would be necessary. Indeed, LOFAR so far has not detected extended polarized emissions from spiral galaxies at frequencies below 200 MHz, probably because of Faraday depolarization. We may have to wait for SKA. Thus, it is necessary to examine how well shape-characterizing parameters will be determined after considering observational effects. We will leave these to future works.

We thank the anonymous referee for constructive comments. S.I. was supported by the National Research Foundation of Korea through grant 2007-0093860. T.A. was supported by JSPS KAKENHI grant numbers 15K17614 and 15H03639. K.T. was supported by Grants-in-Aid from the Ministry of Education, Culture, Sports, Science, and Technology (MEXT) of Japan, Nos. 24340048, 26610048, 15H05896, and 16H05999. D.R. was supported by the National Research Foundation of Korea through grant 2016R1A5A1013277.

Appendix
Calculation of Shape-characterizing Parameters

To derive the width, skewness, and kurtosis in Equations (13)–(15), we employ $F(\phi)$ in Equations (11) and (12) and replace the summation in Equations (3)–(5) with the integration. That is,

$$\begin{aligned}\sum_l |F(\phi_l)| &\rightarrow \int_{-\infty}^{+\infty} |F(\phi)| d\phi \\ &= \int_{-\infty}^{+\infty} \sum_{j=1}^{N_{\parallel}} \frac{1}{\sqrt{2\pi j}\,\sigma_\phi} \exp\left[-\frac{(\phi - j\Delta\phi_{\rm coh})^2}{2j\sigma_\phi^2}\right] d\phi \\ &= \sum_{j=1}^{N_{\parallel}} \int_{-\infty}^{+\infty} \frac{1}{\sqrt{2\pi j}\,\sigma_\phi} \exp\left[-\frac{(\phi - j\Delta\phi_{\rm coh})^2}{2j\sigma_\phi^2}\right] d\phi \\ &= N_{\parallel},\end{aligned} \tag{18}$$

and

$$\begin{aligned}\sum_l |F(\phi_l)|\phi_l &\rightarrow \int_{-\infty}^{+\infty} |F(\phi)|\phi\ d\phi \\ &= \sum_{j=1}^{N_{\parallel}} \int_{-\infty}^{+\infty} \frac{1}{\sqrt{2\pi j}\,\sigma_\phi} \\ &\quad \times \exp\left[-\frac{(\phi - j\Delta\phi_{\rm coh})^2}{2j\sigma_\phi^2}\right] \phi\ d\phi \\ &= \frac{N_{\parallel}(N_{\parallel}+1)}{2}\Delta\phi_{\rm coh}.\end{aligned} \tag{19}$$

Then, the spectrum-weighted average of the Faraday depth becomes

$$\mu = \frac{\sum_j |F(\phi_j)|\phi_j}{\sum_j |F(\phi_j)|} = \frac{N_{\parallel}+1}{2}\Delta\phi_{\rm coh}. \tag{20}$$

In the same manner,

$$\sum_l |F(\phi_l)|(\phi_l - \mu)^2 \to \int_{-\infty}^{+\infty} |F(\phi)|(\phi - \mu)^2 d\phi$$
$$= \sum_{j=1}^{N_\parallel} \int_{-\infty}^{+\infty} \frac{1}{\sqrt{2\pi j}\,\sigma_\phi} \times \exp\left[-\frac{(\phi - j\Delta\phi_{\rm coh})^2}{2j\sigma_\phi^2}\right](\phi - \mu)^2 d\phi$$
$$= \frac{N_\parallel(N_\parallel + 1)(2N_\parallel + 1)}{6}\Delta\phi_{\rm coh}^2 + N_\parallel(N_\parallel + 1)(\sigma_\phi^2 - \mu\Delta\phi_{\rm coh}) + N_\parallel\mu^2. \quad (21)$$

So, the width becomes

$$\sigma^2 = \frac{\sum_j |F(\phi_j)|(\phi_j - \mu)^2}{\sum_j |F(\phi_j)|} = \frac{N_\parallel^2 - 1}{12}\Delta\phi_{\rm coh}^2 + \frac{(N_\parallel + 1)\sigma_\phi^2}{2}. \quad (22)$$

The skewness and kurtosis can be similarly derived.

References

Akahori, T., Ryu, D., Kim, J., & Gaensler, B. M. 2013, ApJ, 767, 150
Armstrong, J. W., Cordes, J. M., & Rickett, B. J. 1981, Natur, 291, 561
Beck, R. 2009, Ap&SS, 320, 77
Beck, R. 2015, A&A, 578, 93
Beck, R. 2016, A&ARv, 24, 4
Beck, R., Frick, P., Stepanov, R., & Sokoloff, D. 2012, A&A, 543, A113
Beck, R., & Wielebinski, R. 2013, in Planets, Stars and Stellar Systems, Vol. 5: Galactic Structure and Stellar Populations, ed. T. D. Oswalt & G. Gilmore (New York: Springer), 641
Bell, M. R., Junklewitz, H., & Ensslin, T. A. 2011, A&A, 535, A85
Brentjens, M. A., & de Bruyn, A. G. 2005, A&A, 441, 1217
Burn, B. J. 1966, MNRAS, 133, 67
Cho, J., & Ryu, D. 2009, ApJL, 705, L90
Farnsworth, D., Rudnick, L., & Brown, S. 2011, AJ, 141, 28
Fletcher, A., Beck, R., Shukurov, A., Berkhuijsen, E. M., & Horellou, C. 2011, MNRAS, 412, 2396
Frick, P., Sokoloff, D., Stepanov, R., & Beck, R. 2011, MNRAS, 414, 2540
Gaensler, B. M., Madsen, G. J., Chatterjee, S., & Mao, S. A. 2008, PASA, 25, 184
Haverkorn, M., Gaensler, B. M., Brown, J. C., et al. 2006, ApJL, 637, L33
Ideguchi, S., Tashiro, Y., Akahori, T., Takahashi, K., & Ryu, D. 2014, ApJ, 792, 51
Krause, M. 2009, RMxAC, 36, 25
Kumazaki, K., Akahori, T., Ideguchi, S., Kurayama, T., & Takahashi, K. 2014, PASJ, 66, 61
Lesieur, M. 1997, Turbulence in Fluids (Dordrecht: Kluwer)
Mao, S. A., Gaensler, B. M., Haverkorn, M., et al. 2010, ApJ, 714, 1170
Miyashita, Y., Ideguchi, S., & Takahashi, K. 2016, PASJ, 68, 44
Mulcahy, D. D., Beck, R., & Heald, G. H. 2017, A&A, 600, 6
Ohno, H., & Shinbata, S. 1993, MNRAS, 262, 953
Orlando, E., & Strong, A. 2013, MNRAS, 436, 2127
Sofue, Y., Machida, M., & Kudoh, T. 2010, PASJ, 62, 1191
Sun, X. H., Rudnick, L., Akahori, T., et al. 2015, AJ, 149, 60
Taylor, A. R., Stil, J. M., & Sunstrum, C. 2009, ApJ, 702, 1230